STScI | SPACE TELESCOPE SCIENCE INSTITUTE

Instrument Science Report ACS 2019-05

SBC Absolute Flux Calibration

R.J. Avila, R. Bohlin, N. Hathi, S. Lockwood, P.L. Lim, M. De La Peña

October 17, 2019

Abstract

The throughput curves for the imaging modes of the Advanced Camera for Surveys Solar Blind Channel (SBC) have been updated to correct for a 15% – 30% error in the absolute flux calibration. The offset is removed by adjusting throughput curves of various components of the different observing modes, and bringing synthetic photometry into agreement with observed photometry. The resulting curves show that the detector is more sensitive than previously estimated. The practical result of these changes is that the new zeropoints are fainter than before. In other words, until now, the observed astrophysical fluxes of sources have been overestimated. Updated zeropoints for F122M and F165LP have accuracies of $\sim 4.5\%$*, while the other filters have accuracies better than* $\sim 1.7\%$*. New throughput curves and other necessary support files have been delivered to the calibration pipeline so that, from now on, SBC images downloaded from MAST contain the appropriate zeropoints.*

1 Introduction

The Solar Blind Channel (SBC) on the Advanced Camera for Surveys (ACS) is a Multi-Anode Microchannel Array (MAMA) photon counting device. It is optimized for observations in the far-ultraviolet (FUV) regime from 1150Å to 1700Å, with a field of view of $35'' \times 31''$, and a plate scale $\sim 0.032''$/pix. It is equipped with a set of six imaging filters (five long-pass and one Lyα filter) and two low-resolution prisms.

The wavelength-dependent throughput curves used for flux calibrations of the SBC imaging mode were first derived during ground testing prior to launch. Tests conducted during the

Servicing Mission Orbital Verification (SMOV) campaign in 2002 showed that the throughput curve for the MAMA detector required wavelength-dependent adjustments (Tran et al., 2003a,b; Sirianni et al., 2003). A revised throughput curve for the detector was delivered in 2008 when a substantial red leak was characterized (Boffi et al., 2008). Figure 1 shows the throughput curves used for each of the SBC imaging modes, as they stood at the beginning of 2019.

In the last few years, observers and STScI staff have noted that the predicted count rates for the imaging modes do not match observed count rates (e.g. Tao et al., 2012; Östlin et al., 2014; Bhattacharyya et al., 2017; Peacock et al., 2018). The ACS Team conducted a campaign with the ultimate aim of fixing the absolute flux calibration of the imaging modes. Recent studies have characterized the dark rate (Avila, 2017; Avila et al., 2018), the aperture corrections (Avila and Chiaberge, 2016), the high-frequency flat fields (Avila et al., 2016), and the low-frequency flat fields and time-dependent sensitivity (TDS; Avila et al. 2019). With these calibrations in hand, it is now possible to undertake a study to derive corrections to the throughput curves, new inverse sensitivities, and new photometric zeropoints.

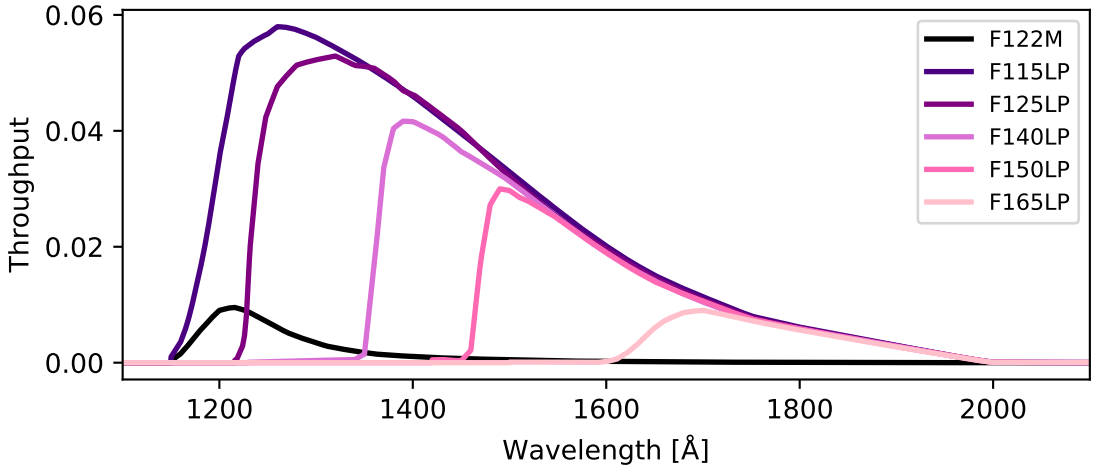

Figure 1: Total system throughput curves for the six imaging modes available on SBC, as they stood in January 2019.

Section 2 presents the data and explains how basic calibration, spectral extraction and photometric measurements were performed. Section 3 describes the synthetic photometry process. Section 4 presents the corrections applied to the throughput curves. Section 5 presents a verification of the corrections. Section 6 presents a discussion of the results and summarizes this report. Section 7 discusses the technical aspects of how these results are being implemented in the calibration pipeline, PYSYNPHOT software , and the observatory Exposure Time Calculator (ETC).

2 Data

SBC photometry and associated UV spectroscopy of sources are necessary in order to determine the absolute flux calibration of an observation mode. These data exist for the open

Table 1: Dataset names of STIS spectra used in this analysis.

Rootname	Proposal ID	Grating	Exposure time [sec]	Observation date
O5JA06030	8422	G140L	800.0	2000-06-21
O5JA06040	8422	G140L	800.0	2000-06-21
O69U09010	8849	G140L	1546.0	2002-06-18
O69U10010	8849	G140L	1546.0	2002-06-20
O5JA06080	8422	G230L	1360.0	2000-06-21
O69U09040	8849	G230L	2588.0	2002-06-18
O69U10040	8849	G230L	2588.0	2002-06-20
O5JA06050	8422	G430L	302.0	2000-06-21
O69U09020	8849	G430L	420.0	2002-06-18
O69U10020	8849	G430L	420.0	2002-06-20

cluster NGC6681. Spectra were obtained with the Space Telescope Imaging Spectrograph (STIS) using a $52'' \times 2''$ long slit, and the FUV/G140L, NUV/G230L, and CCD/G430L modes. Table 1 lists the sets of data included in this analysis. Figure 2 shows the approximate slit alignment on the sky. The locations on the STIS detectors were measured for a dozen relatively well isolated stars, and these spectra were extracted using custom IDL software, as detailed by Bohlin et al. (2019). In particular, clear regions of the images were selected for the sky-background locations. The spectra were extracted with the standard 11 pixel height (0.3 arcsec) for the MAMA FUV and NUV detectors. Wavelengths were assigned based on the distance from the center of the slit for each star; and multiple observations with the same grating were averaged using the exposure times as weights. The STIS/CALSPEC absolute flux calibration is documented in the review by Bohlin et al. (2014). Figure 3 shows the flux distributions for the six brightest and most isolated stars, which were the ones used for this study.

Figure 2: An approximation of the sky location of the STIS slit on the NGC6681 cluster. The marked stars were used for this study. The stars are labeled as in Proffitt et al. (2003). Image was taken with SBC F115LP filter. The image is $2.75'' \times 20''$, and the size of the circles indicate the r=0.5″ (20pixels) apertures used for photometry.

To perform photometry, all SBC images of this field that are available in the Mikulski Archive for Space Telescopes[1] (MAST) were downloaded in RAW format. Failed observations were discarded. Observations where the average detector temperature exceeded 25°C were discarded in order to avoid images with high dark current, which is difficult to correct for in SBC data (Avila, 2017). The final list of images appears in Table 1 of Avila et al. (2019).

[1] `https://mast.stsci.edu`

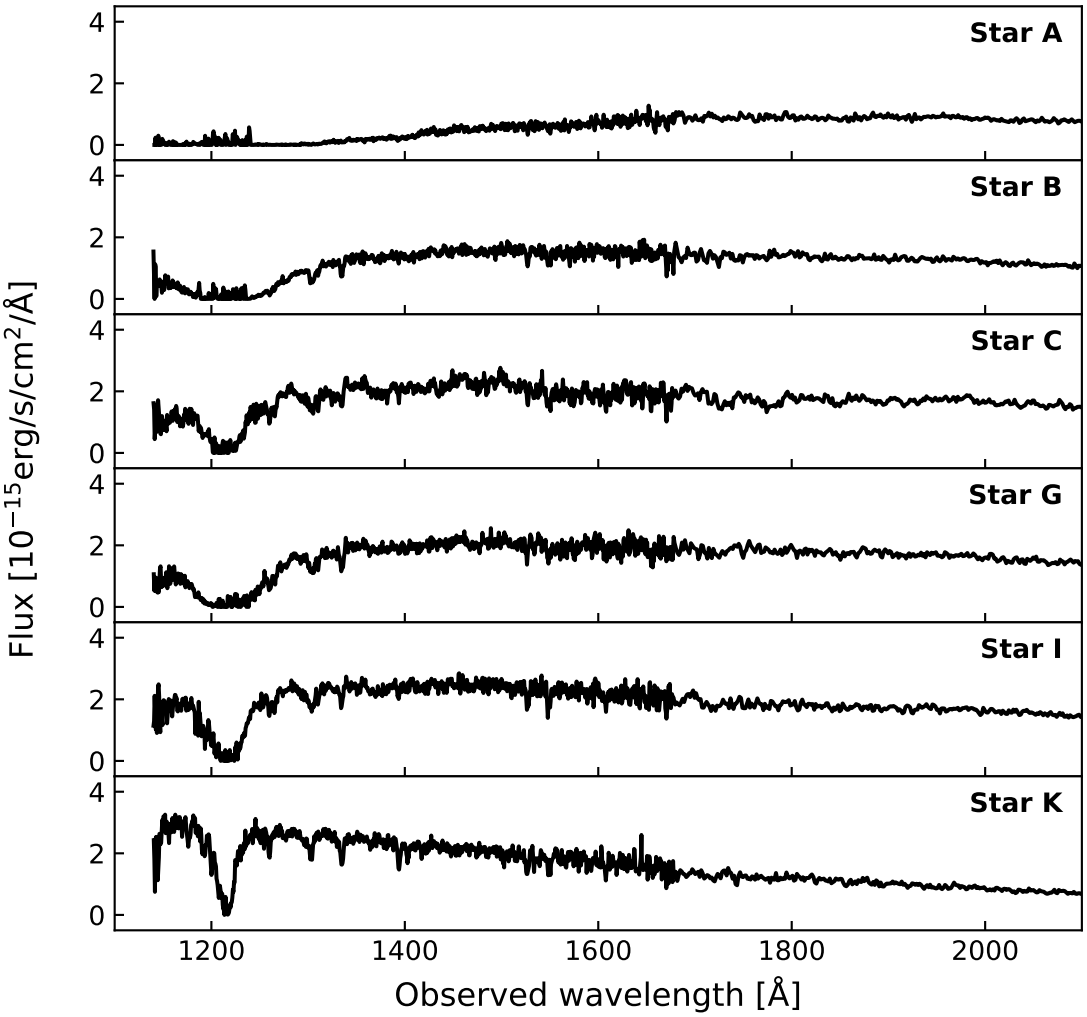

Figure 3: STIS spectra of the six stars used for this analysis, shown in Figure 2. G140L mode was used below 1687Å, and G230L above.

Images were calibrated using the LP-flats derived by Avila et al. (2019).

To define the astrometric grid, it would be ideal to align the SBC images directly to the *Gaia* (Gaia Collaboration et al., 2018) reference frame. Unfortunately, there is no overlap between the SBC images and the *Gaia* catalog because of the small size of the SBC footprint and because *Gaia* does not contain many UV-bright sources. Alignment was accomplished by first aligning near-UV images taken with WFC3/UVIS F275W to *Gaia* and then aligning SBC images to the WFC3/UVIS observations. WFC3 images were from GO-13297 (PI: Piotto), visits 94 and 95.

Calibrated and aligned images (FLT files) were sorted by filter and observation dates. Images taken with the same filter and observation day were drizzled together, and a single world coordinate system (WCS) was used for all drizzled products (see Table 2 of Avila et al. 2019). Photometry was performed on each drizzled image using the aperture_photometry task from the PHOTUTILS (Bradley et al., 2016) package, employing apertures of radius = 0.5″.

Table 2: Number of photometric measurements per star per filter. Star names are the same as Figure 2.

Star	F122M	F115LP	F125LP	F140LP	F150LP	F165LP
A	–	47	50	48	49	47
B	–	47	48	46	48	46
C	9	46	49	47	48	46
G	11	48	48	46	48	46
I	11	47	50	48	48	47
K	11	48	50	48	49	47

Photometry of each star was corrected for TDS effects using the new corrections published by Avila et al. (2019) and further adjusted with aperture corrections from Avila and Chiaberge (2016). Finally, the mean and standard deviation of the photometric measurements of each star were calculated. Photometry of Stars A and B in the F122M filter were discarded because the stars are too faint. Table 2 shows the number of photometric measurements per star per filter.

3 Synthetic Photometry

Synthetic photometry was performed using the PYSYNPHOT python package (Lim et al., 2015). PYSYNPHOT works by using wavelength-dependent throughput curves for every optical component (e.g. mirrors, filter, and detector) in an observing mode. The total throughput function (bandpass) of the requested observing mode is then formed by multiplying together the individual component throughputs at each wavelength.

Table 3: List of throughput curves before corretions.

#	Filename	Component
1	hst_ota_007_syn	optical telescope assembly
2	acs_hrc_m12_006_syn	corrective optics
3	acs_f122m_005_syn	F122M filter
4	acs_f115lp_005_syn	F115LP filter
5	acs_f125lp_006_syn	F125LP filter
6	acs_f140lp_006_syn	F140LP filter
7	acs_f150lp_005_syn	F150LP filter
8	acs_f165lp_005_syn	F165LP filter
9	acs_sbc_mama_009_syn	MAMA detector

Bandpasses are then convolved with observed UV spectra to simulate HST observations of targets, yielding predicted count rates. PYSYNPHOT also has the capability to apply aperture corrections. Table 3 shows the component throughput files that were used in this analysis. The component files that correspond to the observatory and the corrective optics

of the instrument are assumed to be invariable, while the instrument component files can be adjusted.

An example run of synthetic photometry would involve the following steps. The bandpass generator is given the appropriate keywords for the observation mode, for example, `"acs,sbc,f115lp"`. This would take files 1, 2, 4, and 9 from Table 3 and multiply them together. The result would be the throughput curve for F115LP shown in Figure 1. The desired target spectrum is then convolved with the throughput curve. Figure 4 shows the result of this process when applied to Star K. Finally, the convolved spectrum is integrated and converted to the appropriate units to produce a synthetic count rate, which can be compared to observed aperture photometry.

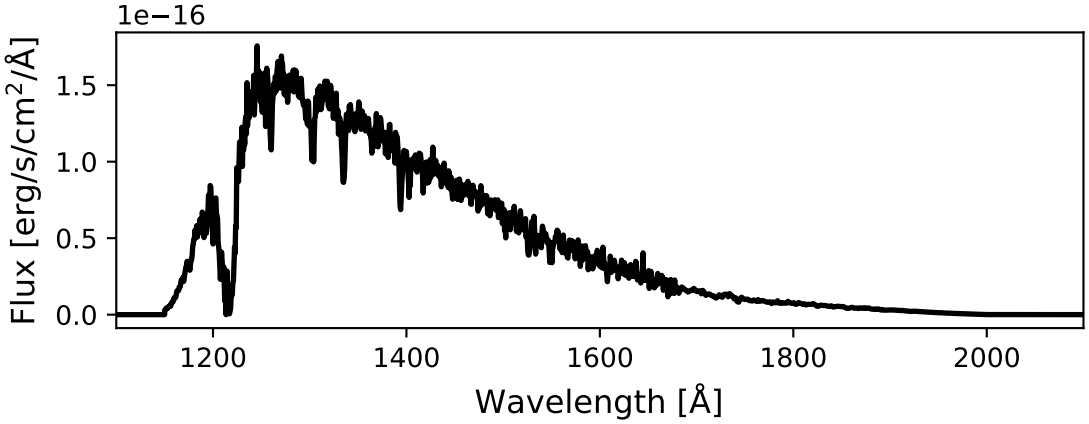

Figure 4: Contributions to the SBC/F115LP total flux as a function of wavelength, i.e. the spectrum of Star K convolved with the system throughput, before corrections were applied.

4 Matched Photometry

Figure 5 shows the ratio of synthetic photometry to observed photometry of each star and filter combination, as a function of the effective wavelength of the observation. The bottom set of points (squares) show the results from using the set of uncorrected throughput curves (Figure 1). The value used for the observed photometry is the mean of all measurements in a filter of each star, and the error bars are the standard deviation of those measurements. The effective wavelength (or mean wavelength of the detected photons) of an observation is defined in Equation 1 (Koornneef et al., 1986). The synthetic photometry deviates from the observed photometry by ∼15% – 33%. The discrepancy is such that the SBC is more sensitive than previously estimated.

$$\lambda_{\text{eff}} = \frac{\int F_\lambda P_\lambda \lambda^2 d\lambda}{\int F_\lambda P_\lambda \lambda d\lambda} \tag{1}$$

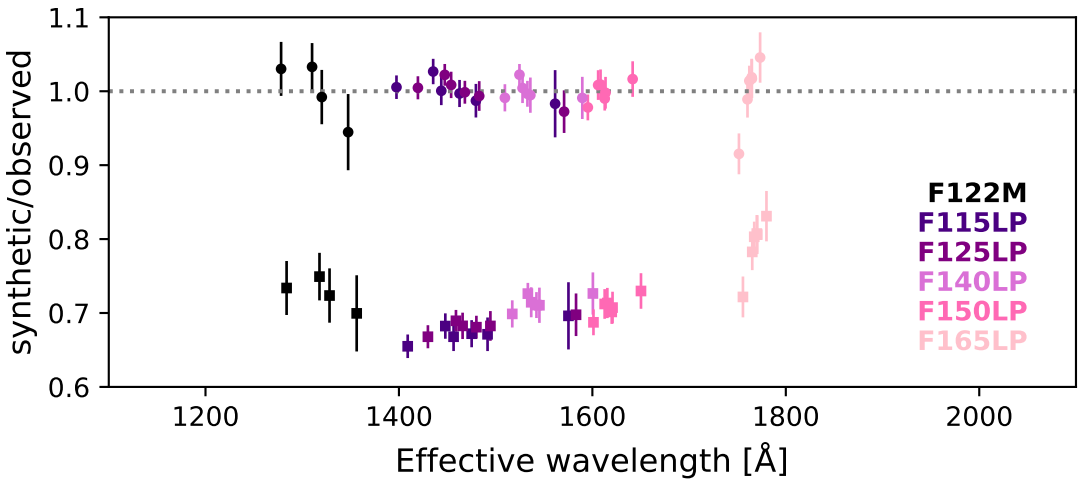

Figure 5: Ratios of synthetic to observed photometry for each star. Square points show the ratios before any adjustments were made to the throughput curves. Circles show the ratios after corrections. Error bars indicate the 1σ scatter in the observed photometry.

Table 4: Residual RMS of the corrected ratios of synthetic to observed photometry by filter.

Filter	Fit residual
F122M	0.041
F115LP	0.015
F125LP	0.017
F140LP	0.012
F150LP	0.014
F165LP	0.045

4.1 Corrections

Adjustments were made to both the detector and filter throughput curves in order to correct the discrepancy between predicted and measured count rates. The detector throughput curve was adjusted first by fitting a line through all the points in Figure 5, except those corresponding to filters F122M and F165LP, and dividing the throughput curve by that line. Tests showed that excluding those two filters yielded more realistic results for the detector throughput curve. With a corrected detector throughput, the synthetic photometry was performed again, and the results compared to the observed photometry. The individual filter throughput curves were adjusted by determining the mean offset of the measurements in each filter. The filter throughput curves were then divided by that constant. The synthetic photometry was run once more, yielding the ratios represented by the top set of points (circles) in Figure 5. Table 4 shows the residual RMS of the final fit for each filter.

The final set of throughput curves for the six imaging modes of the SBC are shown in Figure 6. For comparison, the curves being replaced are shown in dotted lines. The aggregate adjustments resulted in throughput curves with higher sensitivity in all imaging modes.

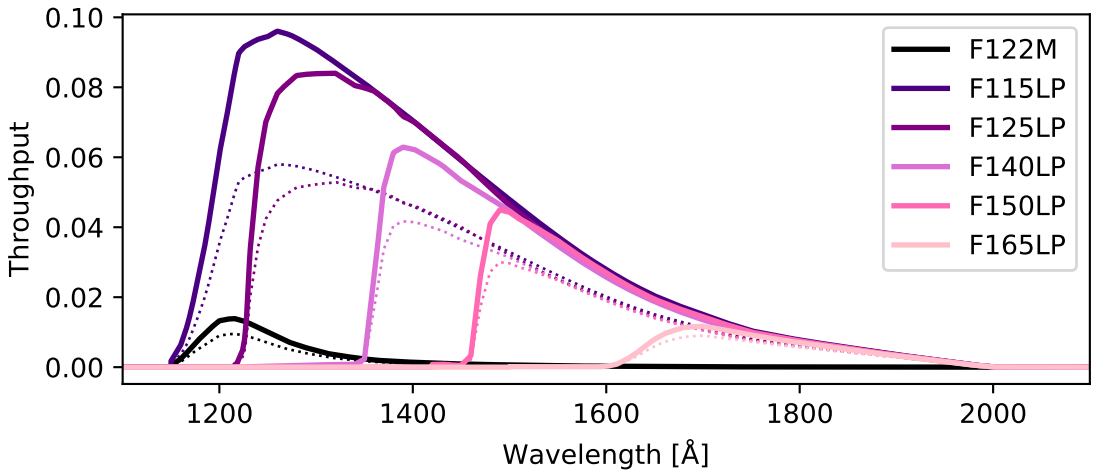

Figure 6: Comparison of the old (dotted) and new (solid) system throughput curves for the six imaging modes.

5 Verification

The new throughput curves were tested by comparing observed and synthetic photometry of a completely different set of stars for which SBC imaging and STIS spectra are available. The list of verification stars and filter combinations used is given in Table 5. These stars are isolated on the sky, so larger 1.″ apertures were used for the photometry. The spectra were obtained from CALSPEC[2], which contains the composite stellar spectra that are flux standards on the HST system.

Figure 7 shows the spectra of verification stars, as well as the ratio of synthetic photometry to observed photometry of each star and filter combination. Square points show the ratio before the throughput curves were corrected. The offset between the observed and synthetic photometry is once again ∼15%–30%. The circles show the results from using the new throughput curves.

Table 5: Stars and filters used to test the new throughput curves.

Star	Filter
HS2027	F122M
LDS749B	F122M
SDSS132811	F125LP
SDSS132811	F140LP
SDSS132811	F150LP
LDS749B	F165LP

[2]http://www.stsci.edu/hst/instrumentation/reference-data-for-calibration-and-tools/astronomical-catalogs/calspec

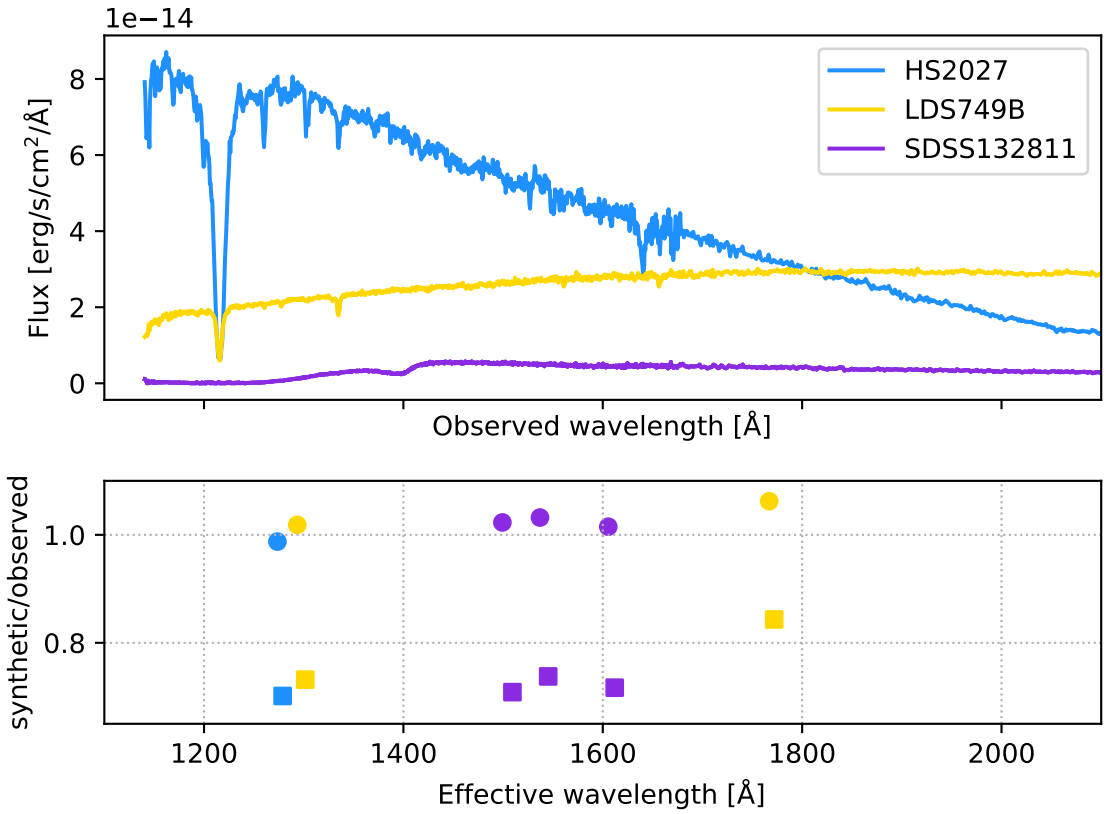

Figure 7: Top) Spectra of stars used for verification. Bottom) Ratios of synthetic and observed photometry for verification stars. Square points correspond to ratios before adjusting the throughput curves. Circles show results after corrections. The colors in the two panels are matched by star.

6 Discussion

Throughput curves for the MAMA detector required an upward adjustment, and additional minor adjustments to the filter curves were also necessary, so that synthetic photometry matched observed photometry. This means that the detector is more sensitive than previously thought – fewer photons are required to produce 1 count per second in a bandpass. Photometry performed on stars that used zeropoints derived from previous curves needs to be made *fainter*. Equivalently, astrophysical fluxes of SBC sources have been *overestimated* in the past.

The residual RMS of the corrected ratios of observed to synthetic photometry shown in Table 4 is below 0.02 in four of the six imaging modes. The residuals for F122M and F165LP fall outside this range because the photometric measurements have low signal to noise. These fit residuals in Table 4 represent the errors in the SBC absolute flux calibration and are consistent with the residual mismatch in the CALSPEC standards seen in Figure 7.

7 Implementation

Zeropoints need to be derived any time adjustments are made to the throughput curves of an imaging mode. The zeropoint of an observing mode is derived by using the inverse sensitivity of the throughput curve, defined as the amount of incident flux required to produce 1 count per second in the given bandpass, with units of erg/second/cm^2/Å. The ACS Data Handbook (Lucas et al., 2018) provides full details on zeropoint derivation. In calibrated images, the inverse sensitivity is stored in the `PHOTFLAM` header keyword. It is not possible to present a single zeropoint for a given observing mode because it depends on the observation date, due to the declining sensitivity with time (Avila et al., 2019). The CALACS software was updated, and the necessary files delivered to the reference pipeline, to enable the capability to update the `PHOTFLAM` keyword with the correct value, depending on the observation date. This capability is present starting with CALACS v10.2.1. All SBC imaging data in MAST will be re-processed with the release of this report, and will be available to users near that time. Alternatively, the ACS Zeropoints Calculator[3] can be used to determine the SBC zeropoints for different photometric systems.

Moving forward, the default behavior of PYSYNPHOT will change when simulating SBC observations. If no observation date is provided to PYSYNPHOT when defining the observing mode, the midpoint date of the next HST cycle will be used.

The ETC also assumes an observation date when providing simulations. Users should consult the ETC release notes[4] to identify what date is being used.

Acknowledgements

The authors would like to thank Marco Chiaberge, Norman Grogin, and Jennifer Mack for their useful discussions on this project. We also thank Yotam Cohen, Tyler Desjardins, Ray Lucas, Melanie Olaes, and Jenna Ryon for their careful review of this report.

This work has made use of data from the European Space Agency (ESA) mission *Gaia* (`https://www.cosmos.esa.int/gaia`), processed by the *Gaia* Data Processing and Analysis Consortium (DPAC, `https://www.cosmos.esa.int/web/gaia/dpac/consortium`). Funding for the DPAC has been provided by national institutions, in particular the institutions participating in the *Gaia* Multilateral Agreement.

This work also made use of the following software packages: `ipython` (Pérez and Granger, 2007), `numpy` and `scipy` (van der Walt et al., 2011), `pandas` (McKinney, 2010), and `matplotlib` (Hunter, 2007).

[3] `https://acszeropoints.stsci.edu`

[4] `https://etc.stsci.edu`

References

R. J. Avila. Updated Measurements of ACS/SBC Dark Rates. Technical report, May 2017.

R. J. Avila and M. Chiaberge. Photometric Aperture Corrections for the ACS/SBC. Technical report, Sep 2016.

R. J. Avila, M. Chiaberge, and R. Bohlin. SBC Internal Lamp P-flat Monitoring. Technical report, Mar 2016.

R. J. Avila, S. Arslanian, M. Bourque, and W. Eck. Mitigating Elevated Dark Rates in SBC Imaging. Technical Report ISR ACS 2018-07, Space Telescope Science Institute, October 2018.

R. J. Avila, M. Chiaberge, D. Kossakowski, and J. Averbukh. SBC Time Dependent Sensitivity and L-flats. Technical Report ISR ACS 2019-04, Space Telescope Science Institute, September 2019.

D. Bhattacharyya, J. T. Clarke, J. L. Bertaux, J. Y. Chaufray, and M. Mayyasi. Analysis and modeling of remote observations of the martian hydrogen exosphere. Icarus, 281: 264–280, Jan 2017. doi: 10.1016/j.icarus.2016.08.034.

F. R. Boffi, M. Sirianni, R. A. Lucas, N. R. Walborn, and C. R. Proffitt. Delivery of a new ACS SBC throughput curve for Synphot. Technical Report ISR ACS 2008-02, Space Telescope Science Institute, April 2008. Available upon request.

R. C. Bohlin, S. E. Deustua, and G. de Rosa. HST Flux Calibration: I. STIS and CALSPEC. AJ, 2019. In press.

Ralph C. Bohlin, Karl D. Gordon, and P. E. Tremblay. Techniques and Review of Absolute Flux Calibration from the Ultraviolet to the Mid-Infrared. PASP, 126(942):711, Aug 2014. doi: 10.1086/677655.

Larry Bradley, Brigitta Sipocz, Thomas Robitaille, Erik Tollerud, Christoph Deil, Zè Vinícius, Kyle Barbary, Hans Moritz Günther, Azalee Bostroem, Michael Droettboom, Erik Bray, Lars Andersen Bratholm, T. E. Pickering, Matt Craig, Sergio Pascual, Johnny Greco, Axel Donath, Wolfgang Kerzendorf, StuartLittlefair, Geert Barentsen, Francesco D'Eugenio, and Benjamin Alan Weaver. astropy/photutils v0.2.2, September 2016. URL `https://doi.org/10.5281/zenodo.155353`.

Gaia Collaboration, A. G. A. Brown, A. Vallenari, T. Prusti, J. H. J. de Bruijne, C. Babusiaux, C. A. L. Bailer-Jones, M. Biermann, D. W. Evans, L. Eyer, and et al. Gaia Data Release 2. Summary of the contents and survey properties. A&A, 616:A1, Aug 2018. doi: 10.1051/0004-6361/201833051.

J. D. Hunter. Matplotlib: A 2d graphics environment. *Computing In Science & Engineering*, 9(3):90–95, 2007.

J. Koornneef, R. Bohlin, R. Buser, K. Horne, and D. Turnshek. Synthetic photometry and the calibration of the Hubble Space Telescope. *Highlights of Astronomy*, 7:833–843, Jan 1986.

P.L. Lim, R.I. Diaz, and V. Laidler. Pysynphot user's guide. `https://pysynphot.readthedocs.io/en/latest/`, 2015. Accessed: 2014-09-21.

R. A. Lucas, T. Desjardins, and et al. *Advanced Camera for Surveys Data Handbook v. 9.0.* February 2018.

Wes McKinney. Data structures for statistical computing in python. In Stéfan van der Walt and Jarrod Millman, editors, *Proceedings of the 9th Python in Science Conference*, pages 51 – 56, 2010.

Göran Östlin, Matthew Hayes, Florent Duval, Andreas Sand berg, Thøger Rivera-Thorsen, Thomas Marquart, Ivana Orlitová, Angela Adamo, Jens Melinder, Lucia Guaita, Hakim Atek, John M. Cannon, Pieter Gruyters, Edmund Christian Herenz, Daniel Kunth, Peter Laursen, J. Miguel Mas-Hesse, Genoveva Micheva, Héctor Otí-Floranes, Stephen A. Pardy, Martin M. Roth, Daniel Schaerer, and Anne Verhamme. The Lyα Reference Sample. I. Survey Outline and First Results for Markarian 259. ApJ, 797(1):11, Dec 2014. doi: 10.1088/0004-637X/797/1/11.

Mark B. Peacock, Stephen E. Zepf, Thomas J. Maccarone, Arunav Kundu, Christian Knigge, Andrea Dieball, and Jay Strader. Hubble Space Telescope FUV observations of M31's globular clusters suggest a spatially homogeneous helium-enriched subpopulation. MNRAS, 481(3):3313–3324, Dec 2018. doi: 10.1093/mnras/sty2461.

Fernando Pérez and Brian E. Granger. IPython: a system for interactive scientific computing. *Computing in Science and Engineering*, 9(3):21–29, May 2007. ISSN 1521-9615. doi: 10.1109/MCSE.2007.53. URL `http://ipython.org`.

C. R. Proffitt, T. M. Brown, B. Mobasher, and J. Davies. Absolute Flux Calibration of STIS MAMA Imaging Modes. Technical report, Jan 2003.

M. Sirianni, G. de Marchi, R. L. Gilliland, R. C. Bohlin, C. Pavlovsky, and J. Mack. On-orbit Sensitivity of ACS. In *HST Calibration Workshop : Hubble after the Installation of the ACS and the NICMOS Cooling System*, page 31, Jan 2003.

Lian Tao, Philip Kaaret, Hua Feng, and Fabien Grisé. The Nature of the UV/Optical Emission of the Ultraluminous X-Ray Source in Holmberg II. ApJ, 750(2):110, May 2012. doi: 10.1088/0004-637X/750/2/110.

H. D. Tran, G. R. Meurer, H. C. Ford, A. R. Martel, M. Sirianni, R. C. Bohlin, M. Clampin, C. Cox, G. de Marchi, G. F. Hartig, R. A. Kimble, and V. Argabright. On-Orbit Performance of the ACS Solar Blind Channel. In *HST Calibration Workshop : Hubble after the Installation of the ACS and the NICMOS Cooling System*, page 86, Jan 2003a.

Hien D. Tran, Gerhardt R. Meurer, Holland C. Ford, Andre R. Martel, Marco Sirianni, Ralph C. Bohlin, Mark Clampin, Colin R. Cox, Guido de Marchi, George F. Hartig, Randy A. Kimble, and Vic S. Argabright. On-orbit performance of the ACS solar blind channel. In J. Chris Blades and Oswald H. W. Siegmund, editors, Proc. SPIE, volume 4854 of *Society of Photo-Optical Instrumentation Engineers (SPIE) Conference Series*, pages 686–693, Feb 2003b. doi: 10.1117/12.474053.

Stéfan van der Walt, S. Chris Colbert, and Gaël Varoquaux. The numpy array: a structure for efficient numerical computation. *CoRR*, abs/1102.1523, 2011. URL `http://arxiv.org/abs/1102.1523`.